Supporting Information File for

Backbone-integrated triplet radicals in linear 2p-3d-4f heterometallic chains and magnetic hysteresis

Shota Tsukii, Nagito Haga, Rina Takano, and Takayuki Ishida*

Department of Engineering Science, The University of Electro-Communications, Chofu, Tokyo 182-8585, Japan
takayuki.ishida@uec.ac.jp

Contents

Experimental Section

Instrumentation

The melting point (Mp.) was recorded using a SANSYO SMP-300. Elemental analysis was performed on a PerkinElmer 2400 II. FT-IR spectra were recorded using a Thermo Scientific Nicolet 6700 spectrometer in the range 4000–400 cm^{-1}. An attenuated total reflection (ATR) method was applied to neat samples. X-ray fluorescence (XRF) spectra were measured on a Rigaku ZSX Primus spectrometer.

Preparation of $\mathbf{1}_{\mathbf{GdCo}}$ - $\mathbf{6}_{\mathbf{YMn}}$

The following procedure is typical. A heptane solution (47 mL) containing $[Tb(hfac)_3(H_2O)_2]$[S1] (40.8 mg; 0.050 mmol) and $[Co(hfac)_2(H_2O)_2]$ (TCI, 25.9 mg; 0.050 mmol) was refluxed until the solvent volume was reduced to 7 mL. A dichloromethane solution (1 mL) containing 5TFPBN[S2] (31.8 mg; 0.100 mmol) was added at 80 °C. After vaporization of dichloromethane had almost ceased, the mixture was allowed to stand at room temperature for one day. The resulting solids were collected by filtration, washed with a small amount of heptane, and air-dried. Polycrystalline $\mathbf{2}_{\mathbf{TbCo}}$ (58.6 mg; 0.031 mmol) was obtained in 62% yield. The products are stable under ambient conditions.

Elemental analysis supports the formula $[RE(hfac)_3(5TFPBN)TM(hfac)_2(5TFPBN)]_n$. No lattice solvent molecules are incorporated. The FT-IR spectra indicate the presence of hfac groups and the absence of water molecules (Fig. S1). XRF measurements confirmed the presence of RE and TM ions (Fig. S2). The data are shown below.

$\mathbf{1}_{\mathbf{GdCo}}$: Yield: 36.9 mg (0.020 mmol, 40%). Mp.: 116.7 – 118.0°C (decomp.). Anal. Calcd. for $C_{55}H_{47}CoGdF_{36}N_4O_{14}$: C, 35.0; H, 2.51; N, 2.97%. Found: C, 35.3; H, 2.59; N, 2.94%. IR (neat, ATR): 1639, 1557, 1530, 1477, 1321, 1252, 1200, 1142, 1099, 881, 803, 795, 741, 698, 691, 669, 660 cm^{-1}.

$\mathbf{2}_{\mathbf{TbCo}}$: Yield: 58.6 mg (0.031 mmol, 62%). Mp.: 120.1 – 122.4°C (decomp.). Anal. Calcd. for $C_{55}H_{47}CoF_{36}N_4O_{14}Tb$: C, 34.50; H, 2.46; N, 2.86%. Found: C, 34.2; H, 2.40; N, 2.89%. IR (neat, ATR): 1640, 1559, 1532, 1478, 1321, 1252, 1200, 1142, 1100, 881, 802, 741, 698, 691, 669, 660 cm^{-1}.

$\mathbf{3}_{\mathbf{DyCo}}$: Yield: 61.0 mg (0.032 mmol, 64%). Mp.: 114.7 – 116.2°C (decomp.). Anal. Calcd. for $C_{55}H_{47}CoDyF_{36}N_4O_{14}$: C, 34.9; H, 2.50; N, 2.96%. Found: C, 34.5; H, 2.24; N, 3.04%. IR (neat,

ATR): 1639, 1557, 1530, 1477, 1321, 1251, 1199, 1130, 1100, 881, 802, 742, 698, 691, 669, 660 cm^{-1}.

4_{GdMn}: Yield: 53.4 mg (0.028 mmol, 56%). Mp.: 107.2 – 107.8°C (decomp.). Anal. Calcd. for $C_{55}H_{47}F_{36}GdMnN_4O_{14}$: C, 35.0; H, 2.50; N, 2.96%. Found: C, 34.8; H, 2.01; N, 3.00%. IR (neat, ATR): 1644, 1557, 1529, 1477, 1318, 1251, 1199, 1142, 1098, 881, 796, 741, 698, 690, 660 cm^{-1}.

5_{TbMn}: Yield: 25.7 mg (0.014 mmol, 27%). Mp.: 105.3 – 106.9°C (decomp.). Anal. Calcd. for $C_{55}H_{47}F_{36}MnN_4O_{14}Tb$: C, 34.6; H, 2.46; N, 2.87 %. Found: C, 34.2; H, 2.40; N, 2.89 %. IR (neat, ATR): 1644, 1557, 1530, 1497, 1477, 1318, 1251, 1197, 1130, 1100, 881, 796, 741, 698, 690, 670 cm^{-1}.

6_{YMn}: Yield: 44.5 mg (0.025 mmol, 50%). M.p.: 105.1 – 107.0°C (decomp.). Anal. Calcd. for $C_{55}H_{47}F_{36}MnN_4O_{14}Y$: C, 36.4; H, 2.61; N, 3.09%. Found: C, 36.1; H, 2.16; N, 3.21%. IR (neat, ATR): 1644, 1557, 1530, 1499, 1478, 1318, 1251, 1199, 1131, 1101, 881, 796, 741, 698, 691, 660 cm^{-1}.

X-ray crystallography

X-ray diffraction data for single crystals of **1_{GdCo}** - **6_{YMn}** were collected on a Rigaku Saturn 70 hybrid pixel array detector with graphite-monochromated Mo Kα radiation (λ = 0.71073 Å). The *hkl* indices and intensity data were processed using CrysAlisPro.[S3] The structures were solved by direct methods and refined using Fourier techniques with the Olex2 1.5 program.[S4] Structural parameters were refined using SHELXL.[S5] Selected crystal data, bond distances, and angles are listed in Tables S1 and S2. For experimental details and full geometrical parameter tables, see CCDC reference numbers 2513513, 2513514, 2513515, 2513516, 2513517, and 2513518 for **1_{GdCo}**, **2_{TbCo}**, **3_{DyCo}**, **4_{GdMn}**, **5_{TbMn}**, and **6_{YMn}**, respectively, where the data were collected at 100 K. CCDC 2535179 contains crystallographic data for **2_{TbCo}** collected at 300 K. The powder X-ray diffraction (PXRD) patterns of these samples were collected using a Rigaku SmartLab Studio II diffractometer with Cu Kα radiation (λ = 1.54178 Å) at room temperature (Fig. S3).

Magnetic measurements

The direct-current (DC) magnetic susceptibilities of **1_{GdCo}** - **6_{YMn}** were measured on a Quantum Design MPMS3 SQUID magnetometer. The susceptibility data were acquired at 0.05 T in a temperature range from 1.8 to 300 K. Magnetization data were recorded at fields of 0–7 T at

1.8 K, and measurements down to 0.4 K were performed using an iQuantum ^{3}He refrigerator option. To avoid a torquing effect, the specimens were fixed with a small amount of eicosane. The magnetic responses were corrected with diamagnetic blank data of a gelatin capsule sample holder and eicosane matrix, measured separately, and further diamagnetic contributions were estimated from Pascal's constants.[S6] The alternating current (AC) susceptibilities were recorded on a Quantum Design PPMS 9T equipped with a DC/AC mag option. The data were acquired with frequencies from 10 Hz to 10 kHz. The temperature dependence was measured upon heating.

DFT calculation

Density functional theory (DFT) calculations were carried out using Gaussian 16, Revision C.01.[S7] The broken-symmetry (BS) approach[S8,S9] was employed to analyze the energy-level structures of two-centered model compounds derived from $\mathbf{4_{GdMn}}$. The 5TFPBN moiety was used to investigate 2p-2p interactions. In the 3d-2p exchange coupling calculations, a two-centered model compound [Mn(H_2O)(hfac)$_2$(5TFPNBH)] was employed, in which one 5TFPNB ligand was replaced by water as a capping ligand, and a distal nitroxide group in the other 5TFPNB was replaced with a hydroxylamine group (namely, 5TFPNBH). Similarly, the 4f-2p exchange coupling was calculated for a two-centered model compound [Gd(H_2O)(hfac)$_3$(5TFPNBH)], where one 5TFPNB was replaced with water, and a distal nitroxide group in the other 5TFPNB was replaced with a hydroxylamine group. Self-consistent field (SCF) energies were calculated using the above geometries. The unrestricted B3LYP functional was used in single-point calculations with a basis set 6-311+G(2d,p),[S10] unless otherwise noted. The exchange coupling constant J in the spin Hamiltonian Eq. (1) was evaluated using Yamaguchi's equation (2).[S11,S12]

$$\hat{H} = -2J\hat{S}_1 \cdot \hat{S}_2 \tag{1}$$

$$J = \frac{E_{\mathrm{BS}}^{\mathrm{LS}} - E^{\mathrm{HS}}}{\langle \hat{S}^2 \rangle^{\mathrm{HS}} - \langle \hat{S}^2 \rangle_{\mathrm{BS}}^{\mathrm{LS}}} \tag{2}$$

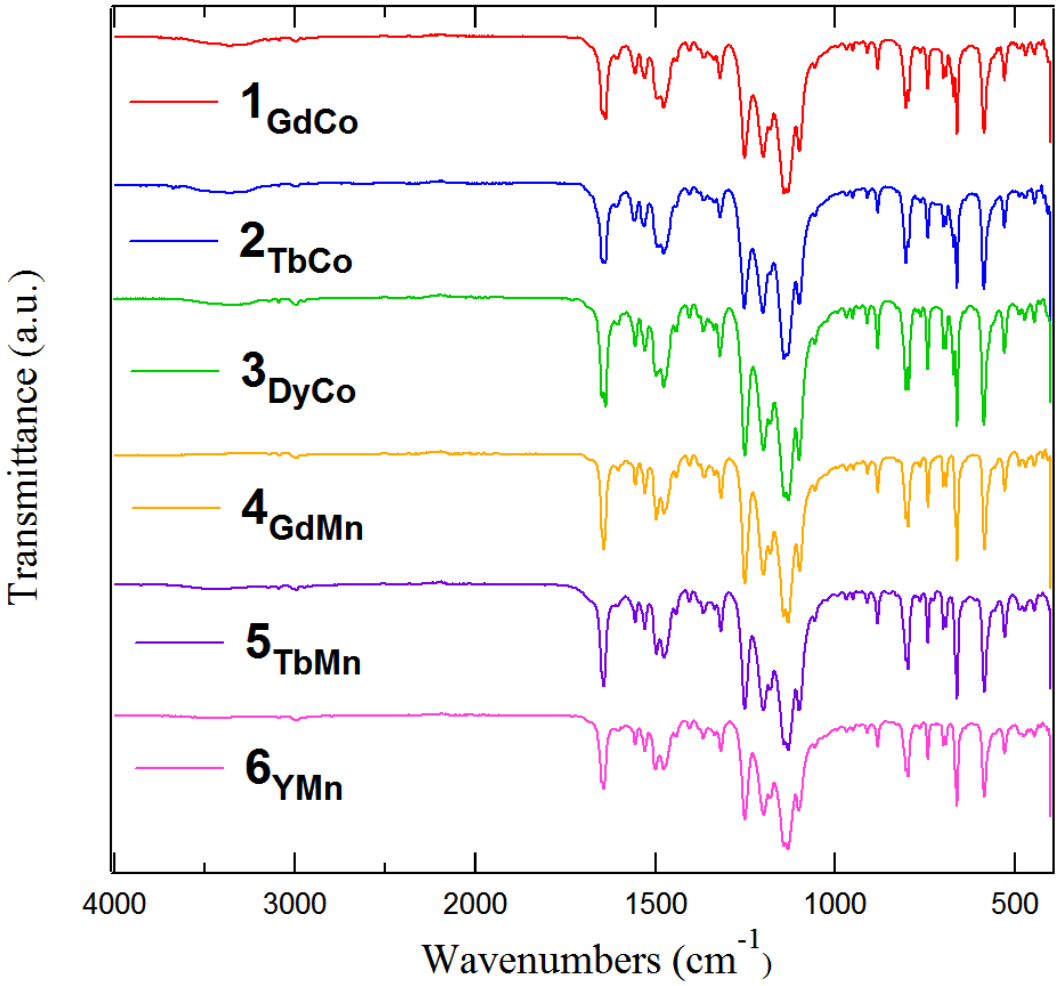

Fig. S1. FT-IR spectra of $\mathbf{1}_{GdCo}$, $\mathbf{2}_{TbCo}$, $\mathbf{3}_{DyCo}$, $\mathbf{4}_{GdMn}$, $\mathbf{5}_{TbMn}$, and $\mathbf{6}_{YMn}$.

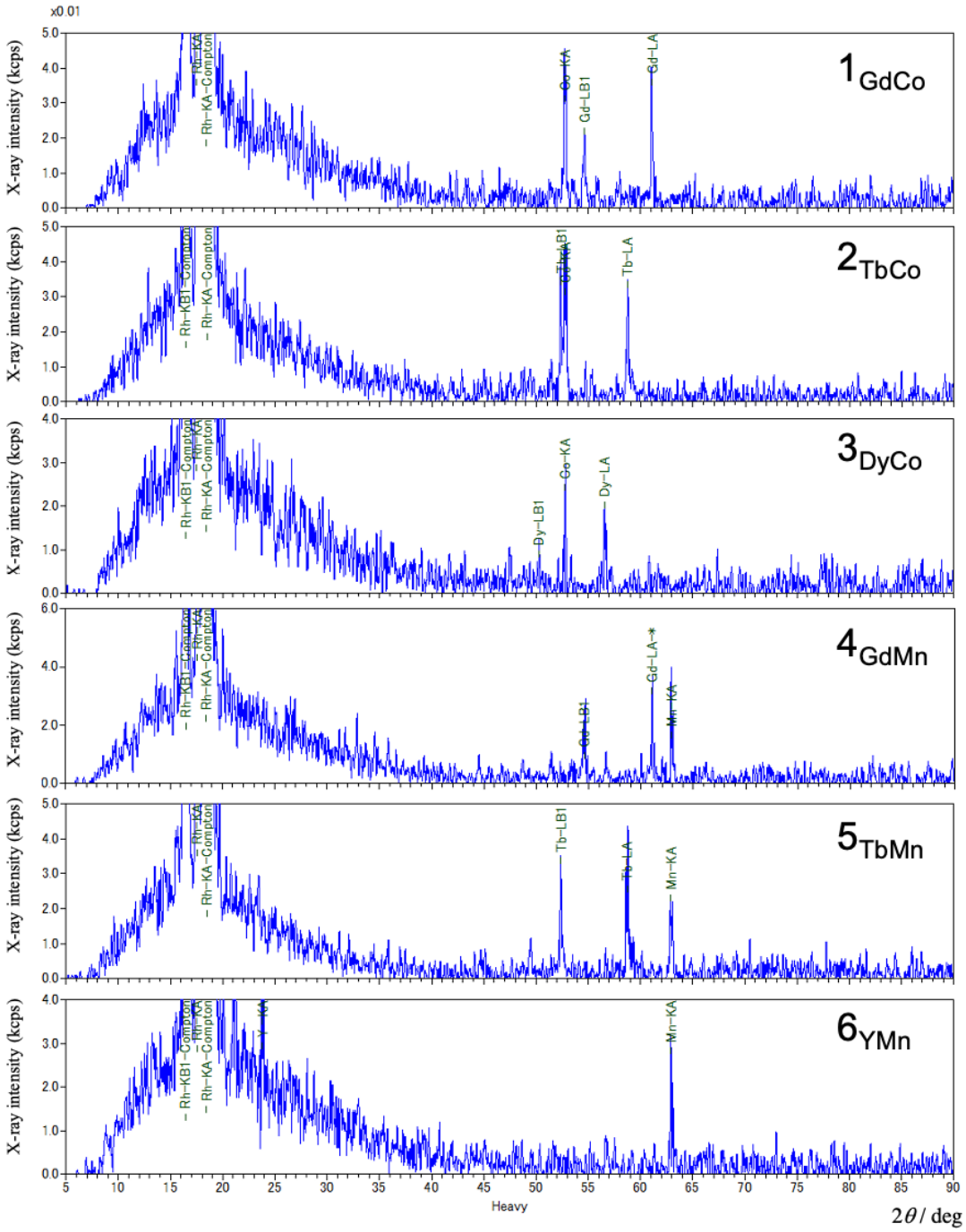

Fig. S2. XRF spectra of $\mathbf{1}_{\mathbf{GdCo}}$, $\mathbf{2}_{\mathbf{TbCo}}$, $\mathbf{3}_{\mathbf{DyCo}}$, $\mathbf{4}_{\mathbf{GdMn}}$, $\mathbf{5}_{\mathbf{TbMn}}$, and $\mathbf{6}_{\mathbf{YMn}}$.

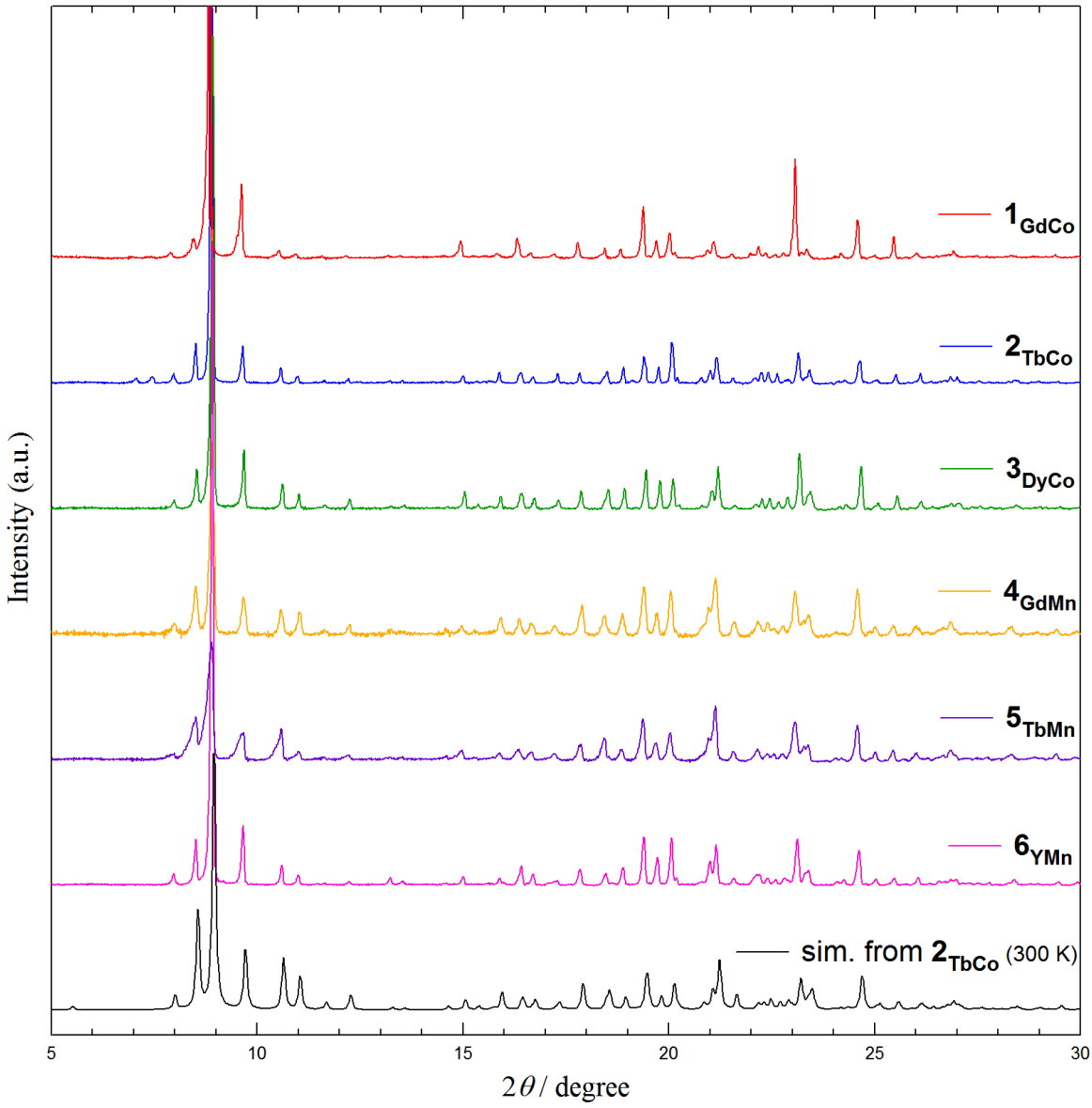

Fig. S3. Experimental PXRD profiles of $\mathbf{1}_{\mathbf{GdCo}}$, $\mathbf{2}_{\mathbf{TbCo}}$, $\mathbf{3}_{\mathbf{DyCo}}$, $\mathbf{4}_{\mathbf{GdMn}}$, $\mathbf{5}_{\mathbf{TbMn}}$, and $\mathbf{6}_{\mathbf{YMn}}$, together with the PXRD pattern simulated from the single-crystal X-ray data of $\mathbf{2}_{\mathbf{TbCo}}$ determined at 300 K.

Table S1. Selected crystallographic parameters of $\mathbf{1}_{\mathbf{GdCo}}$, $\mathbf{2}_{\mathbf{TbCo}}$, $\mathbf{3}_{\mathbf{DyCo}}$, $\mathbf{4}_{\mathbf{GdMn}}$, $\mathbf{5}_{\mathbf{TbMn}}$, and $\mathbf{6}_{\mathbf{YMn}}$.

Compound	$\mathbf{1}_{\mathbf{GdCo}}$	$\mathbf{2}_{\mathbf{TbCo}}$	$\mathbf{3}_{\mathbf{DyCo}}$	$\mathbf{4}_{\mathbf{GdMn}}$	$\mathbf{5}_{\mathbf{TbMn}}$	$\mathbf{6}_{\mathbf{YMn}}$
Formula	C55H47CoF36 GdN4O14	C55H47CoF36 N4O14Tb	C55H47CoDy F36N4O14	C55H47F36Gd MnN4O14	C55H47F36Mn N4O14Tb	C55H47F36Mn N4O14Y
Formula weight	1888.14	1889.81	1893.39	1884.15	1885.82	1815.81
Crystal system	monoclinic	monoclinic	monoclinic	monoclinic	monoclinic	monoclinic
Space group	*C*2/*c*	*C*2/*c*	*C*2/*c*	*C*2/*c*	*C*2/*c*	*C*2/*c*
a / Å	32.3700(4)	32.3702(6)	32.3349(10)	32.2917(12)	32.3437(6)	32.3557(7)
b / Å	11.45068(13)	11.4328(2)	11.4206(5)	11.5050(6)	11.4993(2)	11.4326(3)
c / Å	20.3085(3)	20.2986(4)	20.2951(7)	20.5192(11)	20.4873(4)	20.3954(5)
β / °	96.1372(12)	96.161(2)	96.103(3)	96.216(4)	96.3402(18)	96.403(2)
V / Å^3	7484.36(17)	7468.8(2)	7452.2(5)	7578.4(7)	7573.2(3)	7497.4(3)
Z	4	4	4	4	4	4
d_{calcd} / g·cm^{-3}	1.676	1.681	1.688	1.651	1.654	1.609
μ (MoKα) / mm^{-1}	1.248	1.310	1.367	1.181	1.240	1.087
No. of unique refls.	11156	10917	10305	10396	10587	10485
$R(F)$ ($I > 2\sigma(I)$)[a]	0.0321	0.0338	0.0397	0.0588	0.0417	0.0475
wR (F^2) (all refls.)[b]	0.0693	0.0697	0.0929	0.1696	0.1118	0.1207
GOF parameter	1.041	1.066	1.049	1.052	1.014	1.028
$\Delta\rho_{max}$, $\Delta\rho_{min}$ / e Å^{-3}	0.862, –0.597	0.685, –0.742	0.803, –1.393	1.342, –1.502	1.158, –0.952	1.038, –0.483
T / K	99.9(2)	100.00(14)	99.9(2)	99.9(2)	99.9(2)	99.9(2)
CCDC reference	2513513	2513514[c]	2513515	2513516	2513517	2513518

[a] $R = \Sigma[|F_o| - |F_c|]/ \Sigma|F_o|$. [b] $wR = [\Sigma w(F_o^2 - F_c^2)/\Sigma wF_o^4]^{1/2}$. [C] CCDC reference number for the 300 K data is 2535179.

Table S2. Selected geometrical parameters of $\mathbf{1}_{GdCo}$, $\mathbf{2}_{TbCo}$, $\mathbf{3}_{DyCo}$, $\mathbf{4}_{GdMn}$, $\mathbf{5}_{TbMn}$, and $\mathbf{6}_{YMn}$.[a)]

Compound	$\mathbf{1}_{GdCo}$	$\mathbf{2}_{TbCo}$	$\mathbf{3}_{DyCo}$	$\mathbf{4}_{GdMn}$	$\mathbf{5}_{TbMn}$	$\mathbf{6}_{YMn}$
d / Å						
N1-O1	1.2890(18)	1.285(2)	1.289(2)	1.290(5)	1.286(3)	1.285(2)
N1-C1	1.410(2)	1.410(2)	1.412(3)	1.410(5)	1.411(4)	1.413(3)
N1-C8	1.516(2)	1.516(3)	1.515(3)	1.523(6)	1.521(4)	1.517(3)
N2-O2	1.2951(18)	1.2992(19)	1.299(3)	1.304(4)	1.302(3)	1.303(2)
N2-C5	1.426(2)	1.428(2)	1.432(3)	1.424(5)	1.430(4)	1.425(3)
N2-C12	1.514(2)	1.512(2)	1.507(3)	1.518(6)	1.509(4)	1.510(3)
RE1-O1	2.3680(13)	2.3644(13)	2.3475(16)	2.371(3)	2.369(2)	2.3324(15)
RE1-O3	2.3541(14)	2.3427(17)	2.326(2)	2.348(3)	2.345(3)	2.3123(17)
RE1-O4	2.3596(14)	2.3374(15)	2.3307(18)	2.351(4)	2.338(2)	2.3167(17)
RE1-O5	2.3630(12)	2.3439(14)	2.3285(17)	2.362(3)	2.345(2)	2.3213(16)
TM1-O2	2.0884(12)	2.0882(13)	2.0896(16)	2.115(3)	2.118(2)	2.1168(16)
TM1-O6	2.0621(11)	2.0613(12)	2.0636(16)	2.151(3)	2.1584(19)	2.1518(15)
TM1-O7	2.0187(12)	2.0181(13)	2.0181(18)	2.098(3)	2.099(2)	2.0990(15)
θ / °						
O1-N1-C1	116.57(14)	116.66(16)	116.3(2)	116.7(3)	116.8(2)	116.88(18)
O1-N1-C8	116.75(14)	116.79(15)	117.03(19)	116.8(3)	116.6(2)	116.73(17)
C1-N1-C8	126.50(14)	126.38(15)	126.50(19)	126.2(3)	126.4(2)	126.14(18)
N1-O1-RE1	145.64(11)	145.31(12)	145.79(15)	144.9(3)	144.6(2)	145.67(14)
O1-RE1-O1*	137.19(6)	136.97(7)	137.39(9)	137.41(16)	137.09(11)	137.24(8)
O2-N2-C5	115.19(13)	115.05(14)	115.15(19)	114.8(3)	114.6(2)	114.78(17)

O2-N2-C12	115.24(13)	115.38(14)	115.17(19)	114.7(3)	115.1(2)	114.96(17)
C5-N2-C12	126.16(14)	126.12(15)	126.3(2)	126.9(4)	126.8(2)	126.71(18)
N2-O2-TM1	121.14(10)	121.10(11)	121.22(15)	121.9(2)	121.76(17)	121.32(13)
O2-TM1-O2$^{\#}$	180.0	180.0	180.0	180.0	180.0	180.0
ϕ / °						
O1-N1-C1-C2	22.0(2)	22.0(3)	22.0(3)	21.7(6)	21.4(4)	22.8(3)
O1-N1-C1-C6	–156.50(16)	–157.05(17)	–156.6(2)	–156.4(4)	–156.7(3)	–155.6(2)
O2-N2-C5-C4	138.77(16)	138.89(18)	138.7(2)	138.7(4)	139.1(3)	138.6(2)
O2-N2-C5-C6	–37.2(2)	–37.3(2)	–37.7(3)	–37.0(5)	–37.1(4)	–36.9(3)
RE1-O1-N1-C1	64.6(3)	64.6(3)	64.4(4)	63.3(6)	63.5(4)	61.4(3)
RE1-O1-N1-C8	–119.90(19)	–119.9(2)	–120.5(3)	–122.2(5)	–121.9(3)	–124.0(2)
TM1-O2-N2-C5	–77.63(16)	–77.71(17)	–77.7(2)	–78.3(4)	–78.6(3)	–79.3(2)
TM1-O2-N2-C12	121.89(13)	121.92(15)	121.77(18)	121.2(3)	121.1(2)	120.50(17)

a) Symmetry operation codes of * and $^{\#}$ are (1–x, y, –z+1/2) and (–x+3/2, –y+1/2, –z+1), respectively.

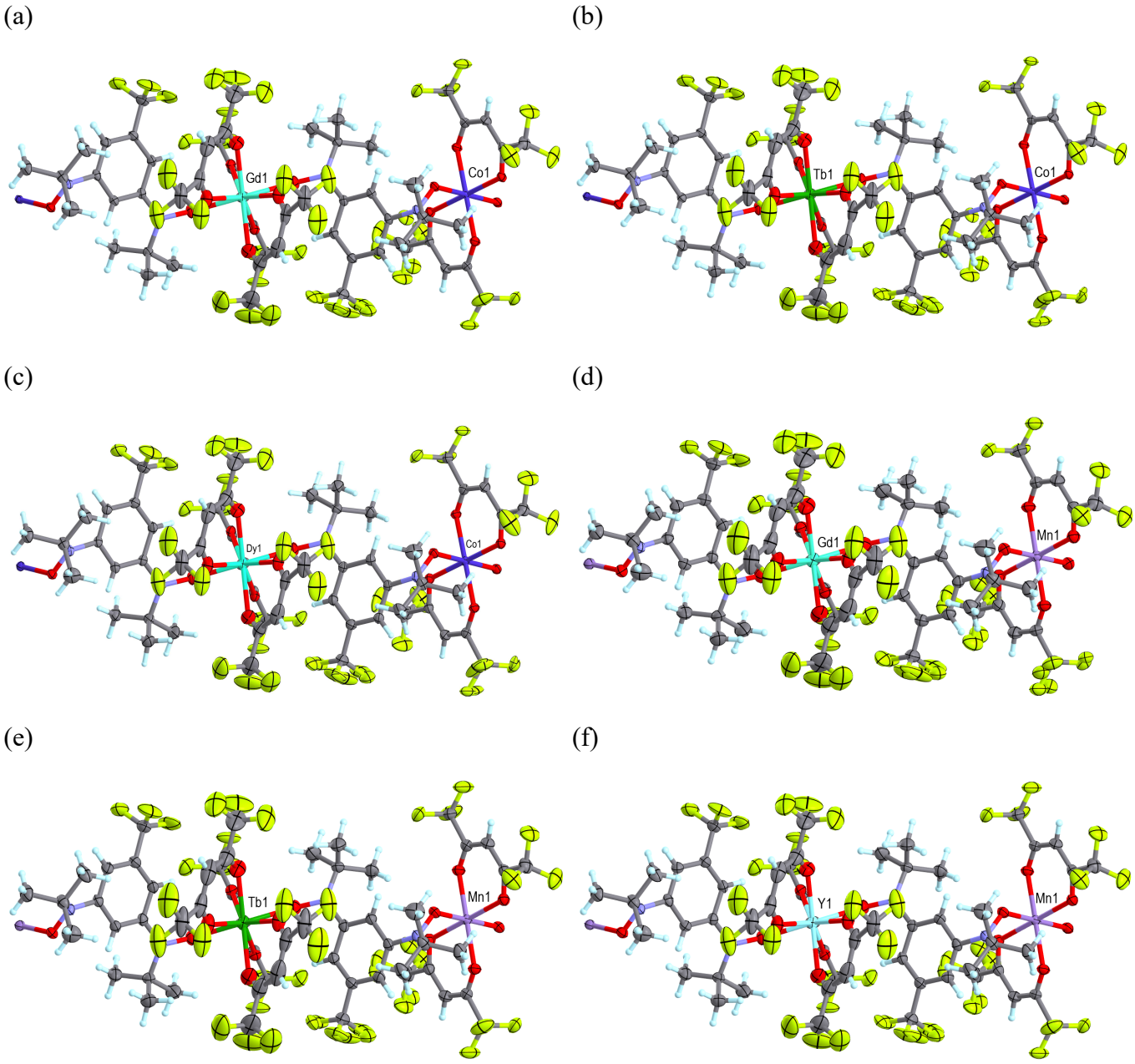

Fig. S4. ORTEP representation of the molecular structure of (a) $\mathbf{1}_{\mathbf{GdCo}}$, (b) $\mathbf{2}_{\mathbf{TbCo}}$, (c) $\mathbf{3}_{\mathbf{DyCo}}$, (d) $\mathbf{4}_{\mathbf{GdMn}}$, (e) $\mathbf{5}_{\mathbf{TbMn}}$, and (f) $\mathbf{6}_{\mathbf{YMn}}$ with thermal ellipsoids drawn at a 50% probability level. The RE and TM ions are labelled. Color codes: C, gray; H, turquoise; N, blue; O, red; F, yellow.

(a)

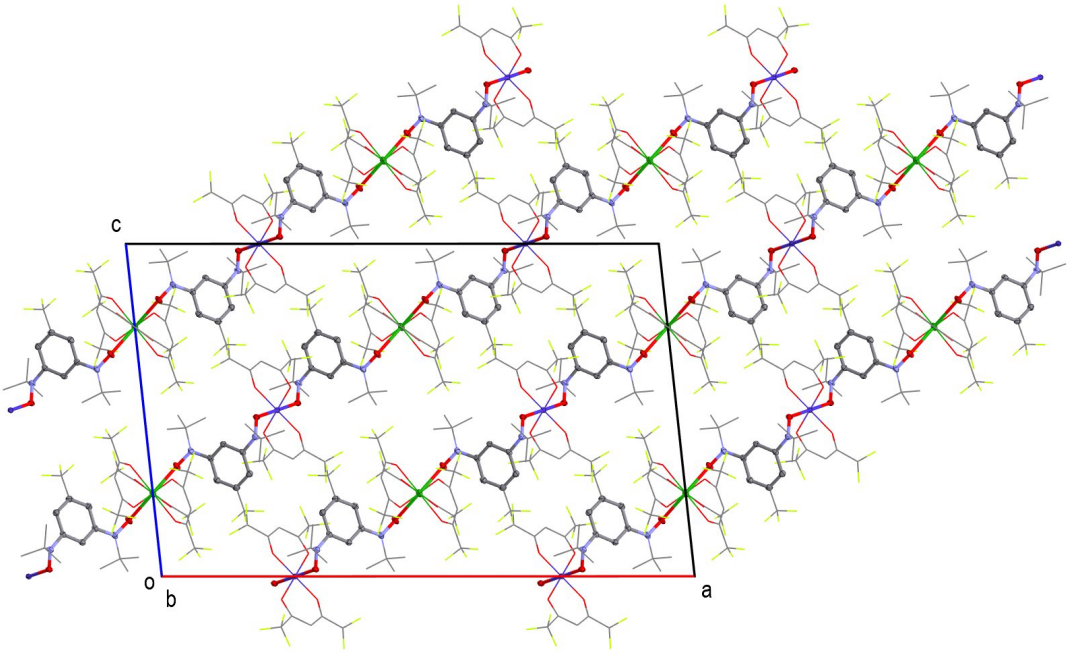

(b)

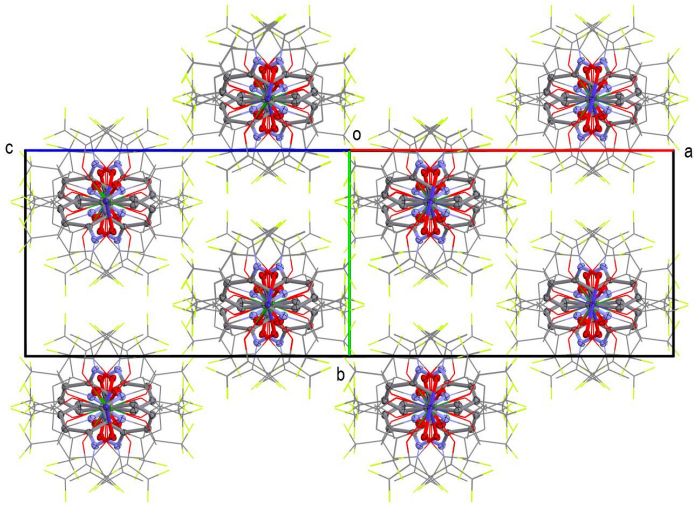

Fig. S5. Molecular packing motif of $\mathbf{2}_{\mathbf{TbCo}}$, (a) viewed in the *b* axis dierction and (b) viewed in the *ac* diagonal direction. The polymer main chain involving Tb^{3+}, Co^{2+} and *m*-phenylene bisnitroxide portions is highlighted. Color codes: Tb, green; Co, purple; C, gray; H, turquoise; N, blue; O, red; F, yellow.

Table S3. SHAPE analysis[S13] for the (a) RE and (b) TM coordination structures in the crystals of **1**$_{GdCo}$ - **6**$_{YMn}$.

(a) RE coordination structures

Label	Symmetry	Shape
OP-8	D_{8h}	Octagon
HPY-8	C_{7v}	Heptagonal pyramid
HBPY-8	D_{6h}	Hexagonal bipyramid
CU-8	O_h	Cube
SAPR-8	D_{4d}	Square antiprism
TDD-8	D_{2d}	Triangular dodecahedron
JGBF-8	D_{2d}	Johnson gyrobifastigium J26
JETBPY-8	D_{3h}	Johnson elongated triangular bipyramid J14
JBTPR-8	C_{2v}	Biaugmented trigonal prism J50
BTPR-8	C_{2v}	Biaugmented trigonal prism
JSD-8	D_{2d}	Snub diphenoid J84
TT-8	T_d	Triakis tetrahedron
ETBPY-8	D_{3h}	Elongated trigonal bipyramid

Structure	OP	HPY	HBPY	CU	SAPR	TDD	JGBF
1$_{GdCo}$ (Gd1)	30.800	23.015	15.784	8.135	0.941	0.666	16.199
2$_{TbCo}$ (Tb1)	30.597	23.116	15.863	8.160	0.889	0.701	16.263
3$_{DyCo}$ (Dy1)	30.565	23.198	15.941	8.264	0.833	0.744	16.176
4$_{GdMn}$ (Gd1)	30.444	23.175	15.749	8.111	0.864	0.701	16.334
5$_{TbMn}$ (Tb1)	30.213	23.114	15.815	8.165	0.806	0.760	16.440
6$_{YMn}$ (Y1)	30.256	23.320	15.878	8.199	0.751	0.810	16.315

Structure	JETBPY	JBTPR	BTPR	JSD	TT	ETBPY
1$_{GdCo}$ (Gd1)	29.130	2.620	2.014	3.618	8.872	24.407
2$_{TbCo}$ (Tb1)	29.169	2.648	2.003	3.729	8.848	24.377
3$_{DyCo}$ (Dy1)	29.205	2.610	1.982	3.725	8.989	24.465
4$_{GdMn}$ (Gd1)	29.139	2.610	1.992	3.675	8.846	24.371
5$_{TbMn}$ (Tb1)	29.084	2.640	1.986	3.802	8.844	24.251
6$_{YMn}$ (Y1)	29.175	2.599	1.980	3.791	8.947	24.404

(b) TM coordination structures

Label	Symmetry	Shape
HP-6	D_{6h}	Hexagon
PPY-6	C_{5v}	Pentagonal pyramid
OC-6	O_h	Octahedron
TPR-6	D_{3h}	Trigonal prism
JPPY-6	C_{5v}	Johnson pentagonal pyramid J2

Structure	HP	PPY	OC	TPR	JPPY
1$_{\mathbf{GdCo}}$ (Co1)	30.840	29.148	0.251	15.710	32.464
2$_{\mathbf{TbCo}}$ (Co1)	30.792	29.120	0.250	15.710	32.430
3$_{\mathbf{DyCo}}$ (Co1)	30.833	29.136	0.248	15.725	32.447
4$_{\mathbf{GdMn}}$ (Mn1)	29.933	28.802	0.343	15.490	32.067
5$_{\mathbf{TbMn}}$ (Mn1)	29.929	28.787	0.351	15.476	32.043
6$_{\mathbf{YMn}}$ (Mn1)	30.188	28.924	0.342	15.457	32.207

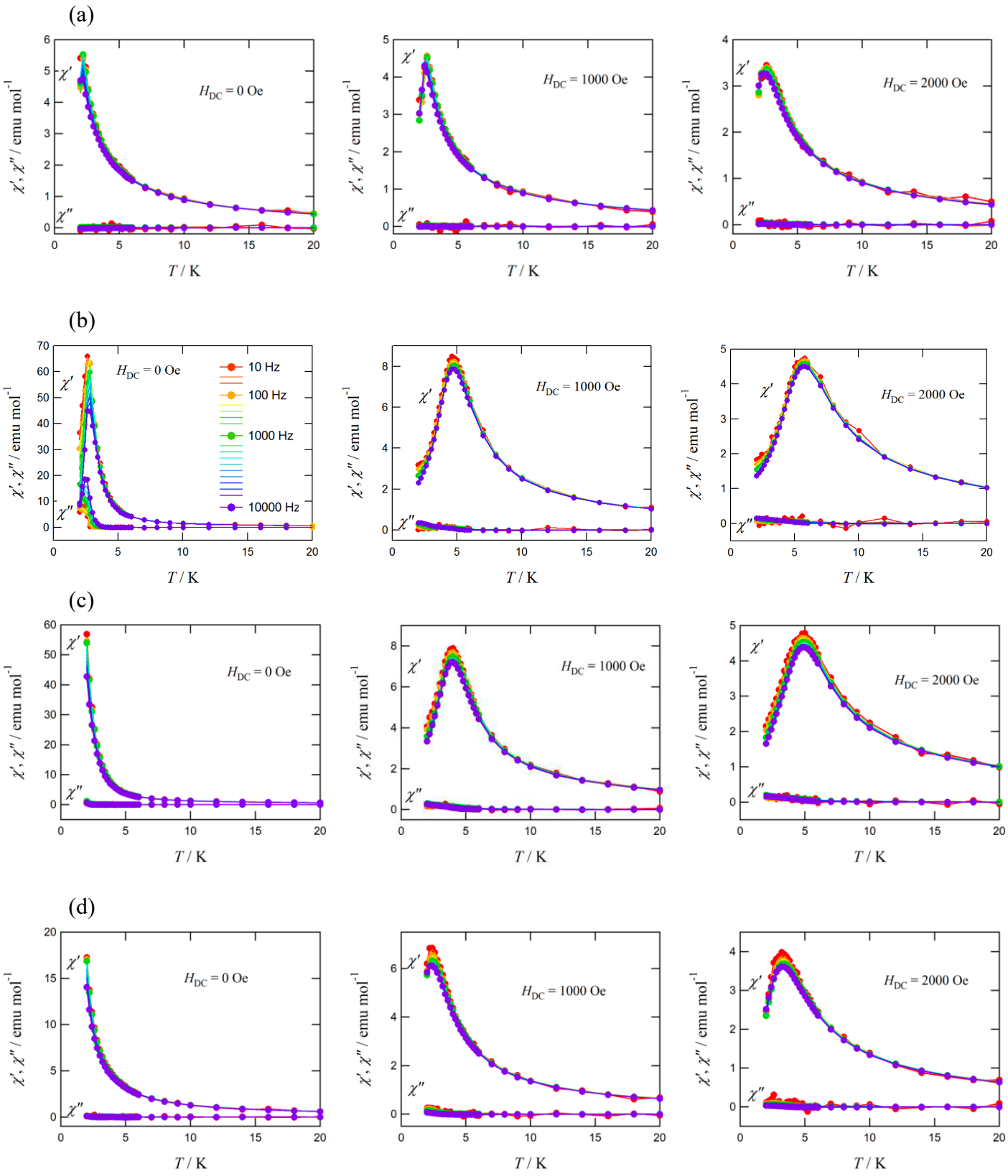

Fig. S6. AC susceptibilities χ' and χ" at DC bias fields of 0.0, 0.1, and 0.2 T for (a) $\mathbf{1}_{\mathbf{GdCo}}$, (b) $\mathbf{2}_{\mathbf{TbCo}}$, (c) $\mathbf{3}_{\mathbf{DyCo}}$, and (d) $\mathbf{5}_{\mathbf{TbMn}}$. For the frequency color codes, see the left panel of (b).

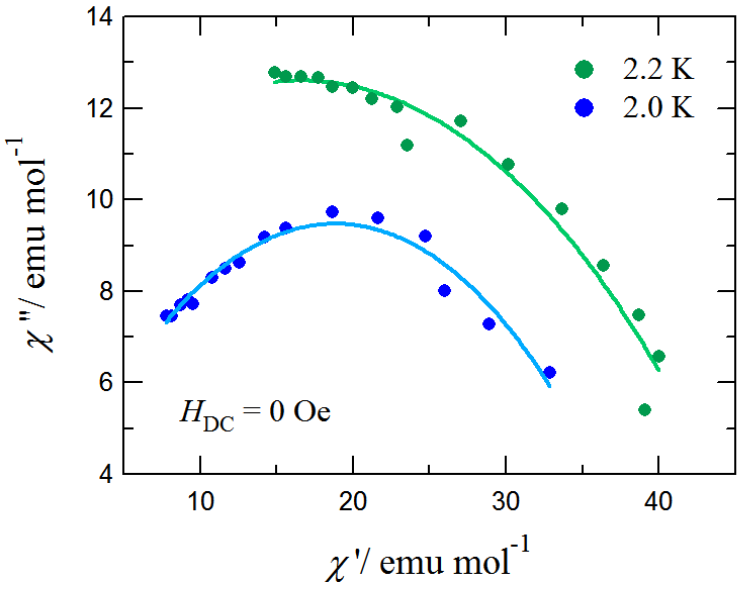

T / K	χ_T / emu mol^{-1}	χ_S / emu mol^{-1}	α
2.0	40.5(8)	–2.8(8)	0.48(2)
2.2	48.4(14)	–15(6)	0.52(5)

Fig. S7. Cole-Cole plot for **2**$_{TbCo}$.

Appendix S1

Simulation details on the magnetic properties of $\mathbf{4}_{\mathbf{GdMn}}$ and $\mathbf{6}_{\mathbf{YMn}}$

The magnetic susceptibility and magnetization data were simulated using the programs MAGPACK[S14] and EasySpin,[S15] which enabled us to propose appropriate exchange-coupling models and to estimate the magnitudes of the relevant magnetic interactions. Estimated errors of the exchange parameters are on the order of 5%.

The exchange-coupled five-centered model employed for $\mathbf{6}_{\mathbf{YMn}}$ is illustrated in Fig. S8a. A macrocyclic approximation involving two repeating units was adopted. To avoid overparameterization, possible next-nearest-neighbor or superexchange interactions, namely $J_{\text{rad-Y-rad}}$ or $J_{\text{rad-Mn-rad}}$, were initially neglected, resulting in a five-centered linear cluster model. The intraligand exchange coupling constant $2J_{\text{rad-rad}}$, estimated from DFT calculations (see below), was incorporated into the model. Subsequent parameter optimization including $J_{\text{rad-Y-rad}}$ yielded the following coupling constants: $2J_{\text{rad-rad}}/k_{\text{B}} = +700$ K and $2J_{\text{Mn-rad}}/k_{\text{B}} = -288$ K together with $2J_{\text{rad-Y-rad}}/k_{\text{B}} = -16$ K, in the spin Hamiltonian $\boldsymbol{H} = -2J\boldsymbol{S}_1\bullet\boldsymbol{S}_2$ convention. A satisfactory fit to the experimental $\chi_{\text{m}}T$-T data was obtained, as shown in Fig. S8c. The corresponding M-H curve simulated with the same parameter set is presented in Fig. S8d.

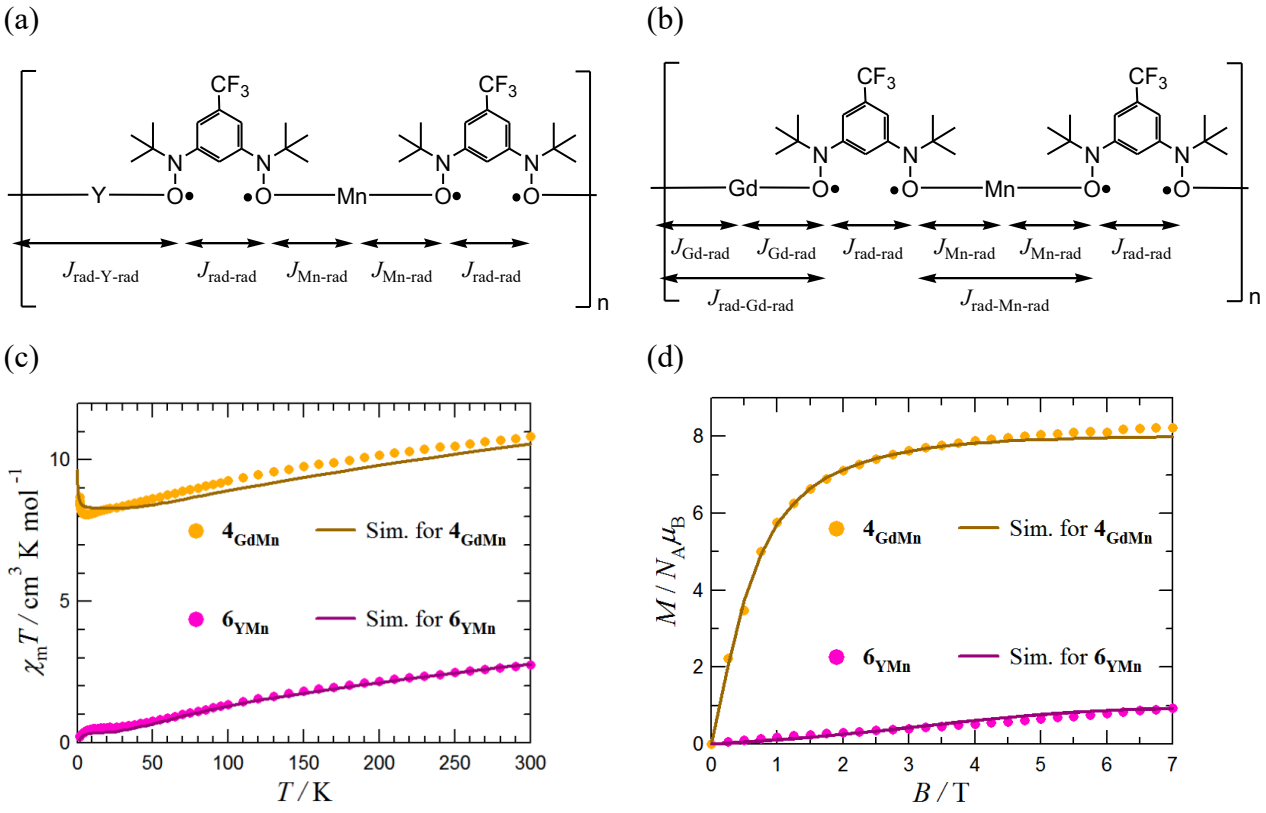

Fig. S8. Exchange-coupling models for (a) $\mathbf{6}_{\mathbf{YMn}}$ and (b) $\mathbf{4}_{\mathbf{GdMn}}$. Experimental data and simulated curves of (c) $\chi_{\text{m}}T$ vs T and (d) M vs H plots for $\mathbf{6}_{\mathbf{YMn}}$ and $\mathbf{4}_{\mathbf{GdMn}}$.

The exchange-coupled six-centered model applied to $\mathbf{4_{GdMn}}$ is shown in Fig. S8b. The same macrocyclic approximation involving two repeating units was used. To avoid overparameterization, possible next-nearest-neighbor or superexchange interactions, such as $J_{\text{rad-Gd-rad}}$ or $J_{\text{rad-Mn-rad}}$, were tentatively omitted. Indeed, the experimental magnetic data are well reproduced using only three exchange parameters, and the inclusion of additional interactions was found to be unnecessary. One representative optimized parameter set is $2J_{\text{rad-rad}}/k_{\text{B}} = +700$ K, $2J_{\text{Mn-rad}}/k_{\text{B}} = -260$ K, and $2J_{\text{Gd-rad}}/k_{\text{B}} = -0.20$ K. Satisfactory fits were obtained for both $\chi_{\text{m}}T$-T and M-H data (Figs. S8c and S8d, respectively). The Gd–rad exchange and rad–Gd–rad superexchange interactions appear to be effectively quenched in this system, consistent with the slight $\chi_{\text{m}}T$ upturn observed at the lowest temperatures. This behavior is likely related to the specific coordination geometry, which results in very weak magnetic coupling.

The following simulations were performed using the EasySpin package.[S15] For $\mathbf{2_{TbCo}}$, the Tb^{3+} ion was treated within an Ising-model approximation as an effective $S = 1/2$ system with $g_{//} \approx 18$.[S16] To simulate the powder magnetic susceptibility, the angular average of the anisotropic g tensor was taken into account by defining an effective value $g_{\text{eff}} = \sqrt{\langle g^2 \rangle}$, which is substantially smaller than the single-crystal easy-axis value $g_{//}$. A similar approximation was applied to the Co^{2+} ion. The $\chi_{\text{m}}T$-T curve calculated using a dimeric macrocycle model reproduced the broad minimum and subsequent low-temperature upturn observed for $\mathbf{2_{TbCo}}$ more accurately when a ferromagnetic Tb-radical interaction was assumed than when an antiferromagnetic one was employed. One representative optimized parameter set is $2J_{\text{rad-rad}}/k_{\text{B}} = +700$ K, $2J_{\text{Tb-rad}}/k_{\text{B}} = +17.3$ K, and $2J_{\text{Co-rad}}/k_{\text{B}} = -144$ K with $S_{\text{Tb}} = 1/2$, $g_{\text{Tb}} = 11.5$, $S_{\text{Co}} = 1/2$, $g_{\text{Co}} = 3.5$, and $g_{\text{rad}} = 2.006$. No next-nearest-neighbor interactions were required to reproduce the experimental behavior. The simulated curve, together with the experimental data, is shown in Fig. S9a. By contrast, omission of $J_{\text{Tb-rad}}$ resulted in an almost constant $\chi_{\text{m}}T$ value below ca. 20 K, whereas an antiferromagnetic $J_{\text{Tb-rad}}$ led to a decrease in $\chi_{\text{m}}T$.

When the organic moiety was treated as an $S = 1$ species, the spin Hamiltonian became slightly simpler, allowing application of a trimeric macrocycle model. Substitution of +8.64 K and −72 K for $2J_{\text{Tb-rad}}/k_{\text{B}}$ and $2J_{\text{Co-rad}}/k_{\text{B}}$, respectively, yielded an improved fit to the experimental data (Fig. S9b). These results strongly support the presence of ferromagnetic Tb-radical interactions.

Similarly, the Dy^{3+} ion in $\mathbf{3_{DyCo}}$ was treated approximately as an effective $S = 1/2$ system with $g_{//} \approx 20$.[S17] The angularly averaged g value is again significantly smaller than the single-crystal easy-axis value $g_{//}$. The simulated $\chi_{\text{m}}T$-T curve based on the same dimeric macrocyclic model successfully

reproduced the broad minimum and the low-temperature upturn observed experimentally. One representative optimized parameter set is $2J_{\text{rad-rad}}/k_B$ = +700 K, $2J_{\text{Dy-rad}}/k_B$ = +31.7 K, and $2J_{\text{Co-rad}}/k_B$ = –144 K with S_{Dy} = 1/2, g_{Dy} = 12.5, S_{Co} = 1/2, g_{Co} = 3.5, and g_{rad} = 2.006. Again, no next-nearest-neighbor interactions were required. A comparison between the simulated and experimental curves is shown in Fig. S10a.

When the organic moiety was treated as an S = 1 species, a trimeric macrocycle model was applied for **3$_{DyCo}$**. Substitution of +15.8 K and –72 K for $2J_{\text{Dy-rad}}/k_B$ and $2J_{\text{Co-rad}}/k_B$, respectively, yielded an improved fit, particularly in the low-temperature $\chi_m T$ upturn region (Fig. S10b). These results strongly suggest the presence of ferromagnetic Dy-radical interactions.

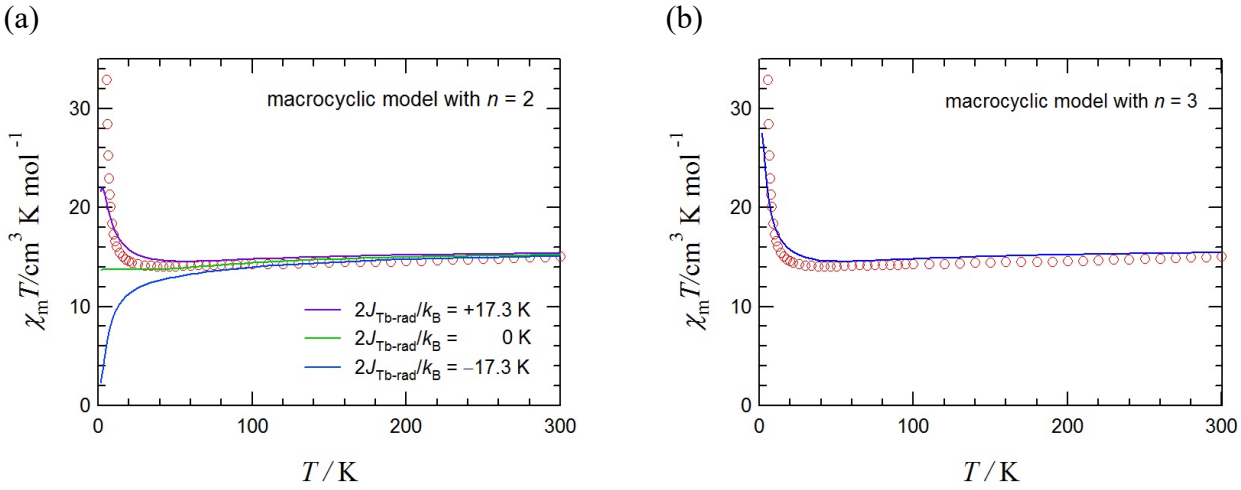

Fig. S9. Simulated $\chi_m T$ vs T curve for **2$_{TbCo}$**: (a) a model containing two S = 1/2 species in the 5TFPBN ligand and (b) a model containing an S = 1 species in the 5TFPBN ligand. See Appendix S1 for the simulation parameters.

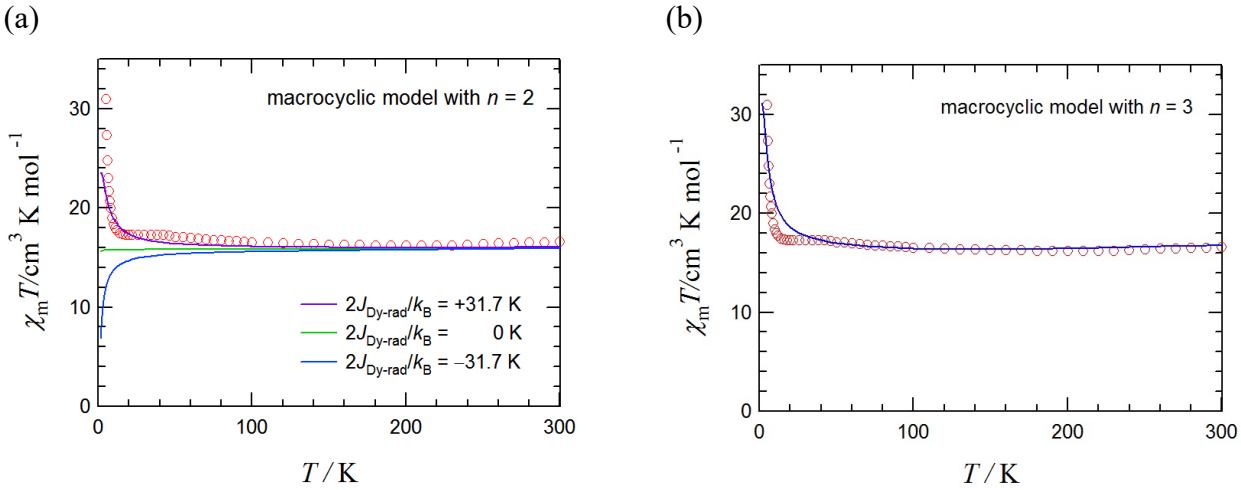

Fig. S10. Simulated $\chi_m T$ vs T curve for **3$_{DyCo}$**: (a) a model containing two S = 1/2 species in the 5TFPBN ligand and (b) a model containing an S = 1 species in the 5TFPBN ligand. See Appendix S1 for the simulation parameters.

Appendix S2

DFT calculation details for $\mathbf{4_{GdMn}}$

The experimentally determined atomic coordinates for $\mathbf{4_{GdMn}}$ were subjected to density functional theory (DFT) calculations using Gaussian 16.[S7] The self-consistent field (SCF) energies were evaluated at the unrestricted level. Computational details are provided in the Experimental section.

First, the electronic ground state of 5TFPBN is of primary importance in this study, because steric prohibition of resonance between the benzene ring and the two nitroxide groups governs the intramolecular radical-radical exchange coupling. As a result, large ferromagnetic coupling constants, $2J_{\text{rad-rad}}/k_{\text{B}}$ = +718 and +566 K, were obtained using the UB3LYP and UM06-2X functionals, respectively, with the 6-311G+(2p,d) basis set for the 5TFPBN moiety in $\mathbf{4_{GdMn}}$, thus indicating a triplet ground state (Tables in Fig. S10a1 and S10a2). These results are consistent with the proposed magneto-structural relationship.[S18,S19] The corresponding spin density maps are also shown.

Next, the 3d-2p exchange coupling was evaluated using a two-center model compound, [Mn(H_2O)(hfac)$_2$(5TFPNBH)], in which one 5TFPNB ligand was replaced by a water molecule as a capping ligand, and the distal nitroxide group of the remaining 5TFPNB ligand was replaced by a hydroxylamine group, yielding 5TFPNBH. The atomic coordinates were extracted from those of $\mathbf{4_{GdMn}}$, and only the additional atoms were geometry-optimized at the UB3LYP/6-311G+(2p,d) level. After applying the LANL2DZ basis set to Mn^{2+}, the quintet ground state and septet excited state were confirmed, with $2J_{\text{Mn-rad}}/k_{\text{B}}$ = –952 and –650 K at the UB3LYP and UM06-2X/6-311G+(2p,d) levels, respectively (Fig. S10b1 and S10b2). These results clearly indicate strong antiferromagnetic coupling with a large energy gap.

Finally, the 4f-2p exchange coupling was examined using a two-center model compound, [Gd(H_2O)(hfac)$_3$(5TFPNBH)], constructed analogously to the 3d-2p model, in which one 5TFPNB ligand was replaced by water and the distal nitroxide group of the other 5TFPNB ligand was replaced by a hydroxylamine group. Although validation of DFT approaches for lanthanide systems remains an ongoing challenge, Chibotaru noted in 2015 that, in the case of Gd^{3+}, "DFT methods may work."[S20] Upon applying the SDD (Stuttgart/Dresden) quasi-relativistic effective core potential to Gd^{3+},[S21,S22] the nonet ground state and septet excited state were obtained, giving $2J_{\text{Gd-rad}}/k_{\text{B}}$ = +7.99 and +14.99 K at the UB3LYP and UM06-2X/6-311G+(2p,d) levels, respectively (Fig. S10c1 and S10c2). These results suggest weak ferromagnetic coupling.

In comparison with the experimental results, the discrepancy between experiment and calculation likely reflects limitations of the DFT treatment for 4f–2p exchange interactions. Nevertheless, the calculations support the proposed magneto-structural relationship: the out-of-plane torsion angle around the Gd-O-N-C(sp^2) in $\mathbf{4_{GdMn}}$ is significantly larger than the critical angle $|\phi_c| = 40(2)°$,[S23,S24] at which the exchange interaction changes from ferro- to antiferromagnetic. The experimentally determined torsion angle of 63.3(6)° lies in the ferromagnetic region. It should be noted that the calculations were performed for isolated molecules in vacuum, which differs from the actual crystalline environment. Steric effects from the bulky polymeric backbone and electronic effects from neighboring substituents may therefore influence the exchange coupling. The simulation results indicate a very small antiferromagnetic interaction, which may arise from an intrinsic ferromagnetic interaction perturbed by such steric and electronic effects.

(a1) $J_{\text{rad-rad}}$ (UB3LYP/6-311G+(2p,d))

	SCF energy	$< S^2 >$	$2J_{\text{rad-rad}} / k_B$
Triplet	–1143.74812387697 au	2.0223	+718.46 K
Singlet	–1143.74697207975 au	1.0104	

Triplet Singlet

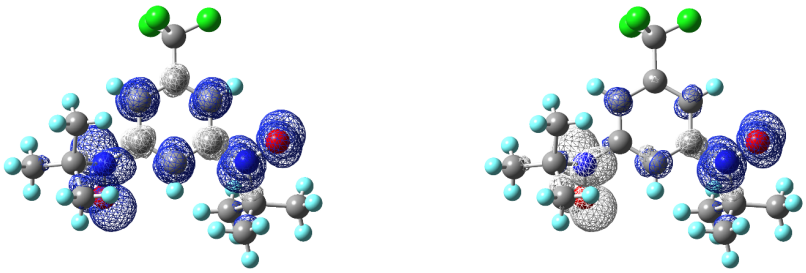

(a2) $J_{\text{rad-rad}}$ (UM06-2X/6-311G+(2p,d))

	SCF energy	$< S^2 >$	$2J_{\text{rad-rad}} / k_B$
Triplet	–1143.29513830366 au	2.0230	+565.97 K
Singlet	–1143.29423303095 au	1.0134	

Triplet Singlet

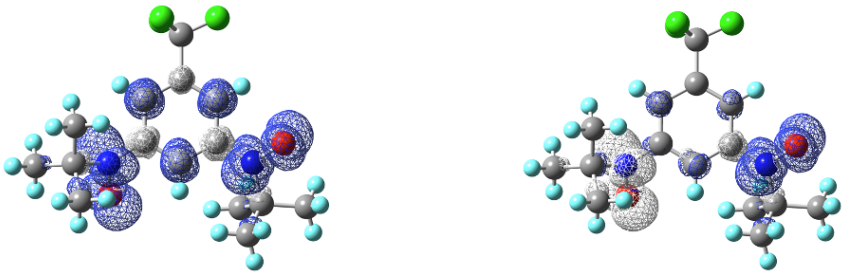

(b1) $J_{\text{Mn-rad}}$ (UB3LYP/6-311G+(2p,d) and Lanl2dz for Mn)

	SCF energy	$< S^2 >$	$2J_{\text{Mn-rad}} / k_B$
Septet	–3206.77528527010 au	12.0116	–952.28 K
Quintet	–3206.78301197688 au	6.8901	

Septet

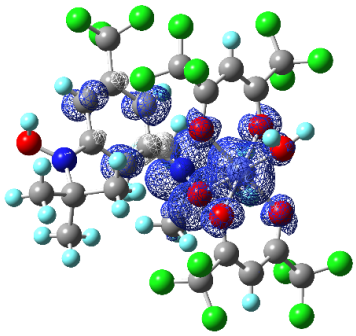

Quintet

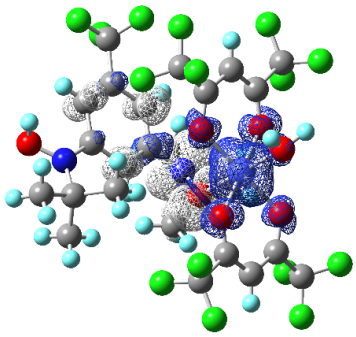

(b2) $J_{\text{Mn-rad}}$ (UM06-2X/6-311G+(2p,d) and Lanl2dz for Mn)

	SCF energy	$< S^2 >$	$2J_{\text{Mn-rad}} / k_B$
Septet	–3205.72242743858 au	12.0109	–649.82 K
Quintet	–3205.72762663805 au	6.96070	

Septet

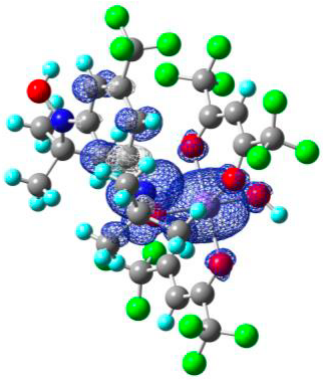

Quintet

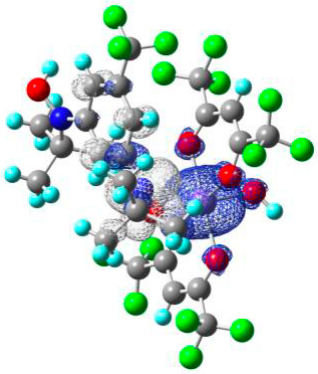

(c1) $J_{Gd\text{-}rad}$ (UB3LYP/6-311G+(2p,d) and SDD for Gd)

	SCF energy	$< S^2 >$	$2J_{Gd\text{-}rad} / k_B$
Nonet	–4809.67856333719 au	20.206	+7.99 K
Septet	–4809.67847470083 au	13.0182	

Nonet Septet

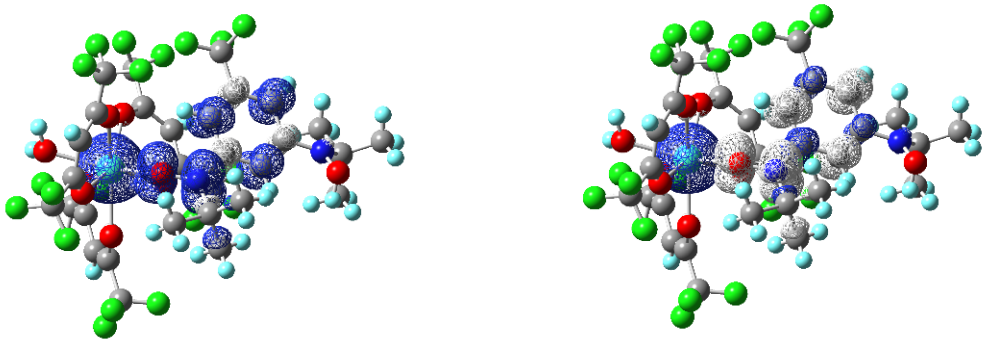

(c2) $J_{Gd\text{-}rad}$ (UM06-2X/6-311G+(2p,d) and SDD for Gd)

	SCF energy	$< S^2 >$	$2J_{Gd\text{-}rad} / k_B$
Nonet	–4808.32498455059 au	20.0246	+14.99 K
Septet	–4808.32481819943 au	13.0238	

Nonet Septet

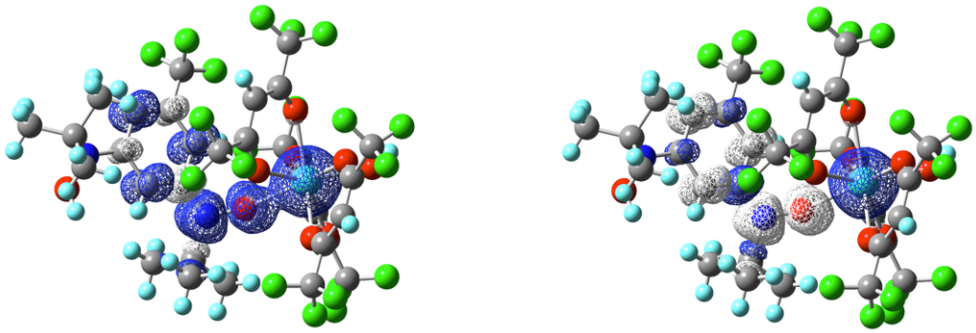

Fig. S11. Energy levels and spin densities for the calculations of (a1,a2) $J_{rad\text{-}rad}$, (b1,b2) $J_{Mn\text{-}rad}$, and (c1,c2) $J_{Gd\text{-}rad}$ in $\mathbf{4}_{\mathbf{GdMn}}$.

References

S1 M. F. Richardson, W. F. Wagner and D. E. Sands, *J. Inorg. Nucl. Chem.*, 1968, **30**, 1275.

S2 N. Haga and T. Ishida, *Tetrahedron*, 2025, **179**, 134614.

S3 CrysAlisPRO, Oxford Diffraction/Agilent Technologies UK Ltd, Yarnton, England.

S4 O. V. Dolomanov, L. J. Bourhis, R. J. Gildea, J. A. K. Howard and H. Puschmann, *J. Appl. Crystallogr.*, 2009, **42**, 339.

S5 G. M. Sheldrick, *Acta Crystallogr., Sect. C: Struct. Chem.*, 2015, **71**, 3.

S6 G. A. Bain and J. F. Berry, *J. Chem. Educ.*, 2008, **85**, 532.

S7 Gaussian 16, Revision C.01, M. J. Frisch, G. W. Trucks, H. B. Schlegel, G. E. Scuseria, M. A. Robb, J. R. Cheeseman, G. Scalmani, V. Barone, G. A. Petersson, H. Nakatsuji, X. Li, M. Caricato, A. V. Marenich, J. Bloino, B. G. Janesko, R. Gomperts, B. Mennucci, H. P. Hratchian, J. V. Ortiz, A. F. Izmaylov, J. L. Sonnenberg, D. Williams-Young, F. Ding, F. Lipparini, F. Egidi, J. Goings, B. Peng, A. Petrone, T. Henderson, D. Ranasinghe, V. G. Zakrzewski, J. Gao, N. Rega, G. Zheng, W. Liang, M. Hada, M. Ehara, K. Toyota, R. Fukuda, J. Hasegawa, M. Ishida, T. Nakajima, Y. Honda, O. Kitao, H. Nakai, T. Vreven, K. Throssell, J. A. Montgomery, Jr., J. E. Peralta, F. Ogliaro, M. J. Bearpark, J. J. Heyd, E. N. Brothers, K. N. Kudin, V. N. Staroverov, T. A. Keith, R. Kobayashi, J. Normand, K. Raghavachari, A. P. Rendell, J. C. Burant, S. S. Iyengar, J. Tomasi, M. Cossi, J. M. Millam, M. Klene, C. Adamo, R. Cammi, J. W. Ochterski, R. L. Martin, K. Morokuma, O. Farkas, J. B. Foresman, and D. J. Fox, Gaussian, Inc., Wallingford CT, 2019.

S8 L. Noodleman and J. G. Norman Jr., *J. Chem. Phys.*, 1979, **70**, 4903.

S9 L. Noodleman, *J. Chem. Phys.*, 1981, **74**, 5737.

S10 J. B. Foresman and Æ. Frisch, *Exploring Chemistry with Electronic Structure Methods*, 3rd edn., Gaussian Inc., Wallingford, CT, USA, 1996.

S11 K. Yamaguchi, Y. Toyoda and T. Fueno, *Synth. Met.*, 1987, **19**, 81.

S12 T. Soda, Y. Kitagawa, T. Onishi, Y. Takano, Y. Shigeta, H. Nagao, Y. Yoshioka and K. Yamaguchi, *Chem. Phys. Lett.*, 2000, **319**, 223.

S13 M. Llunell, D. Casanova, J. Cirera, J. M. Bofill, P. Alemany, S. Alvarez, M. Pinsky and D. Avnir, SHAPE, v2.1, University of Barcelona, Barcelona, Spain and The Hebrew University of Jerusalem, Jerusalem, Israel, 2005.

S14 J. J. Borrás-Almenar, J. M. Clemente-Juan, E. Coronado, B. S. Tsukerblat, *J. Comput. Chem*. 2001, **22**, 985.

S15 S. Stoll and A. Schweiger, *J. Magn. Reson.* 2006, **178**, 42.

S16 J. E. McPeak, S. S. Eaton and G. R. Eaton and G. R. *Electron paramagnetic resonance of lanthanides. In Methods in enzymology*, 2021, **651**, 63-101.

S17 M. Perfetti, M. Gysler, Y. Rechkemmer-Patalen, P. Zhang, H. Taştan, F. Fischer, J. Netz, W. Frey, L. W. Zimmermann, T. Schleid, M. Hakl, M. Orlita, L. Ungur, L. Chibotaru, T. Brock-Nannestad, S. Piligkos, J. van Slageren and J. van Slageren, *Chem. Sci.*, 2019, **10**, 2101.

S18 V. Barone, C. Boilleau, I. Cacelli, A. Ferretti and G. Prampolini, *J. Chem. Theory Comput.*, 2013, **9**, 1958.

S19 N. Haga and T. Ishida, *Molecules*, 2024, **29**, 70.

S20 L. Ungur and L. F. Chibotaru, in *Lanthanides and Actinides in Molecular Magnetism*, ed. R. A. Layfield and M. Murugesu, Wiley-VCH Verlag GmbH & Co. KGaA, Weinheim, Germany, 2015.

S21 I. Dias, L. Gano, S. Chaves and M. A. Santos, *Molecules*, 2025, **30**, 1295.

S22 M. Travadi, R. N. Jadeja and R. J. Butcher, *ACS Omega*, 2022, **7**, 34359.

S23 T. Kanetomo, Y. Naoi and M. Enomoto, *Eur. J. Inorg. Chem.*, 2021, **2021**, 1130.

S24 T. Kanetomo, T. Yoshitake and T. Ishida, *Inorg. Chem.*, 2016, **55**, 8140.